Acta Geophysica (2020) 68:1–17
https://doi.org/10.1007/s11600-019-00377-0

RESEARCH ARTICLE - SOLID EARTH SCIENCES

Seismic time–frequency spectrum analysis based on local polynomial Fourier transform

Pengfei Qi[1] · **Yanchun Wang**[1]

Received: 12 July 2019 / Accepted: 4 October 2019 / Published online: 13 November 2019

Abstract

Time–frequency analysis technology is widely used in non-stationary seismic data analysis. The energy concentration of the spectrum depends on the consistency of the kernel function of the time–frequency analysis method and the instantaneous frequency variation of the signals. The conventional time–frequency analysis methods usually require that the local instantaneous frequency of the signals remains unchanged or linearly changed. So it is difficult to accurately characterize the instantaneous frequency nonlinear variation of the non-stationary signal. The local polynomial Fourier transform (LPFT) method can effectively describe the instantaneous frequency variation by local high-order polynomial fitting and obtain the results with high spectral and energy concentration. The numerical simulations and field seismic data applications show that the time–frequency spectrum results obtained by LPFT can reflect the instantaneous frequency variation characteristics of the seismic data, while ensuring the concentration of time–frequency energy.

Keywords Non-stationary seismic data · Time–frequency analysis · Local polynomial Fourier transform · Energy concentration

Introduction

Numerous studies have indicated that seismic waves vary continuously with increasing propagation distance due to the influence of geometric diffusion, absorption attenuation and fluid, resulting in the non-stationary seismic data (e.g., Rene et al. 1986; Wang 2006; Wang et al. 2012; Yuan et al. 2017). Time–frequency analysis technique is an effective approach of non-stationary signals characterization. By transforming the one-dimensional signal in the time domain into the time–frequency domain, the relationship between the frequency components over time can be characterized (Puryear et al. 2012; Liu et al. 2016; Yuan et al. 2019a).

Traditional time–frequency analysis methods include short-time Fourier transform (STFT) (Durak and Arikan 2003), continuous wavelet transform (CWT) (Sinha et al. 2009), S transform (ST) (Wu and Castagna 2017), matching pursuit (MP) (Mallat and Zhang 1993), etc. STFT realizes the characterization of the time–frequency relationship of non-stationary signals by calculating the Fourier transform of the truncated signal in the time window. However, its time window function is fixed, and the time–frequency resolution is the same regardless of the low-frequency or the high-frequency components. So STFT belongs to the single-resolution analysis method (Zhong and Huang 2010). To conquer the shortcomings of single-resolution STFT, CWT and ST make use of variable time windows instead of fixed ones. The time window is adjusted automatically by the methods. Wider time windows are used for the low-frequency components, while narrower time windows are used for the high-frequency components, thereby realizing multi-resolution analysis of the signal (Phinyomark et al. 2011; Li et al. 2016). As a different approach, the MP method adopts the time–frequency atomic dictionary instead of the time window function. The waveform and width of the atom are defined based on the instantaneous frequency (IF), instantaneous phase and envelope of the local signal. Then the multi-resolution analysis of the signal is realized by Wigner–Ville distribution (Wang 2010). So far, these time–frequency analysis methods have been widely applied in seismic exploration, such as high resolution processing (Smith et al. 2008; Radad et al. 2015), denoising (Parolai 2009;

✉ Yanchun Wang
wangyc@cugb.edu.cn

[1] School of Geophysics and Information Technology, China University of Geosciences, Beijing 100083, China

Ouadfeul and Aliouane 2014), structural interpretation (Wang et al. 2019), reservoir prediction (Partyka et al. 1999; Naseer and Asim 2017) and hydrocarbon detection (Sun et al. 2002; Castagna et al. 2003; Yuan et al. 2019b).

In fact, the traditional time–frequency analysis method implies the hypothesis of quasi-stationary in application (Kadambe and Boudreaux-Bartels 1992) that the statistical features of non-stationary signal does not change in the local time domain. Therefore, these methods are essentially zero-order fitting of the time–frequency features. That is, based on the orthogonal rectangular time–frequency grid, the line segments parallel to the time axis or the frequency axis are used to approximate the time–frequency characteristics of the signal in the local time–frequency plane (Yang et al. 2014). Take STFT for example, its basis function is sine or cosine function, the instantaneous frequency in the time window remains unchanged. It may lead to poor concentration of time–frequency energy and difficult to accurately delineate the local time–frequency characteristics of non-stationary signals.

To weaken the prerequisite of quasi-stationary, Mann and Haykin (1995) proposed a linear chirplet transform (LCT) method that allows the time–frequency grid to be tilted. The characterization of time–frequency features of non-stationary signals was improved by using a line segment with a certain slope in the local time–frequency plane to approximate the time–frequency characteristics of signals. However, since the slope parameter of the chirplet in the LCT is fixed, the time–frequency energy spectrum with higher concentration can be obtained only when the slope value is the same as the local time–frequency slope of the signal. In order to adapt to different time–frequency tilt variations, Yu and Zhou (2016) generalized this method and proposed the general linear chirplet transform (GLCT) method. The key of GLCT is to scan the slope values of the chirplet at local time–frequency points to obtain time–frequency energy with different concentrations and to select the slope value corresponding to the highest energy concentration as the time–frequency slope of the current time–frequency point. Therefore, the LCT and GLCT methods are essentially the first-order fitting of the local time–frequency characteristics of the signal. Accurate analysis results can be achieved especially when the local time–frequency characteristics of the non-stationary signal conform to linear variation.

Actually the local time–frequency characteristics of non-stationary signals tend to vary nonlinearly. Therefore, Katkovnik (1998) proposed the local polynomial Fourier transform (LPFT) method, which allows the time–frequency grids to generate the local curvature. High-order characterization of local time–frequency variations of signals is achieved by polynomial fitting. LPFT can accurately characterize the IF variation of signals with high time–frequency energy concentration (Li et al. 2011).

In this paper, firstly, the LPFT method is analyzed on the basis of the analytical signal expression of Ville (1948). The calculation process of the coefficients in polynomial demodulation operator is given as well. Then, through the synthetic data, we compare LPFT methods with the traditional time–frequency analysis methods, such as STFT, CWT, ST and MP. Finally, LPFT is applied to the real seismic data, which verifies the validity of the method.

Methods

According to Ville (1948) theory, an analytical signal $s(t)$ can be expressed as

$$s(t) = A(t)\exp\left[i\int f(t)\mathrm{d}t\right], \tag{1}$$

where t represents time, $A(t)$ represents instantaneous amplitude, $f(t)$ represents instantaneous frequency (IF), i represents the imaginary unit, and the integral result represents instantaneous phase.

The STFT of the signal $s(t)$ can be expressed as (Cohen 1995)

$$\begin{aligned} S(\tau,\omega) &= \int_{-\infty}^{\infty} w(t-\tau)s(t)\exp(-i\omega t)\mathrm{d}t \\ &= \int_{-\infty}^{\infty} w(t-\tau)A(t)\exp(-i\omega t)\exp\left[i\int f(t)dt\right]\mathrm{d}t \end{aligned}, \tag{2}$$

where $S(\tau, \omega)$ represents the time–frequency spectrum at time τ and frequency ω, and $w(t-\tau)$ represents the time window.

According to the Taylor formula, the IF $f(t)$ can be Taylor expanded in the time window $w(t-\tau)$ as

$$f(t) = f(\tau) + \sum_{k=1}^{n}\frac{1}{k!}f^{(k)}(\tau)(t-\tau)^k + R_n(t), \tag{3}$$

where ! represents the factorial, $f^{(k)}(\tau)$ represents the kth derivative of $f(t)$ at time τ, $R_n(t)$ represents the Lagrangian remainder, and n represents the order of the Taylor expansion. Ignore $R_n(t)$ and substitute Eq. (3) into (2), we have

$$\begin{aligned} S(\tau,\omega) &= \int_{-\infty}^{\infty} w(t-\tau)A(t)\exp(-i\omega t)\exp \\ &\quad\times\left\{i\left[f(\tau)t + \sum_{k=1}^{n}\frac{1}{k!\cdot(k+1)}f^{(k)}(\tau)(t-\tau)^{k+1}\right]\right\}\mathrm{d}t. \end{aligned} \tag{4}$$

Therefore, the amplitude at the time–frequency point (τ, $f(\tau)$) can be expressed as

$$
\begin{aligned}
|S(\tau,f(\tau))| &= \left|\int_{-\infty}^{\infty} w(t-\tau)\exp\left(-if(\tau)t\right)A(t)\exp\right. \\
&\quad\left.\times\left\{i\left[f(\tau)t+\sum_{k=1}^{n}\frac{1}{k!\cdot(k+1)}f^{(k)}(\tau)(t-\tau)^{k+1}\right]\right\}\mathrm{d}t\right| \\
&= \left|\int_{-\infty}^{\infty} w(t-\tau)A(t)\exp\right. \\
&\quad\left.\times\left\{i\left[\sum_{k=1}^{n}\frac{1}{k!\cdot(k+1)}f^{(k)}(\tau)(t-\tau)^{k+1}\right]\right\}\mathrm{d}t\right| \\
&\le \left|\int_{-\infty}^{\infty} w(t-\tau)A(t)\mathrm{d}t\right|
\end{aligned}
\tag{5}
$$

Due to the presence of the modulation component in Eq. (5)

$$
\exp\left\{i\left[\sum_{k=1}^{n}\frac{1}{k!\cdot(k+1)}f^{(k)}(\tau)(t-\tau)^{k+1}\right]\right\}, \tag{6}
$$

the time–frequency amplitude at $(\tau, f(\tau))$ is reduced, which makes the amplitude of STFT unable to focus on the $f(t)$. To achieve that the amplitude maxima are obtained at $(\tau, f(\tau))$ so that the time–frequency spectrum obtains a higher time–frequency energy concentration, it is necessary to eliminate the exponential term in Eq. (6). Therefore, a polynomial demodulation operator is introduced into STFT,

$$
\exp\left\{-i\left[\sum_{k=1}^{n}\frac{1}{k!\cdot(k+1)}c_k(\tau)(t-\tau)^{k+1}\right]\right\}, \tag{7}
$$

where c_k is the coefficient of the polynomial demodulation operator.

Thus, Eq. (2) becomes

$$
\begin{aligned}
S(\tau,\omega) &= \int_{-\infty}^{\infty} w(t-\tau)s(t)\exp(-i\omega t) \\
&\quad\times\exp\left\{-i\left[\sum_{k=1}^{n}\frac{1}{k!\cdot(k+1)}c_k(\tau)(t-\tau)^{k+1}\right]\right\}\mathrm{d}t,
\end{aligned}
\tag{8}
$$

and

$$
\begin{aligned}
S(\tau,f(\tau)) &= \int_{-\infty}^{\infty} w(t-\tau)s(t)\exp\left(-if(\tau)t\right)\exp \\
&\quad\times\left\{-i\left[\sum_{k=1}^{n}\frac{1}{k!\cdot(k+1)}c_k(\tau)(t-\tau)^{k+1}\right]\right\}\mathrm{d}t \\
&= \int_{-\infty}^{\infty} w(t-\tau)A(t)\exp \\
&\quad\times\left\{i\left[\sum_{k=1}^{n}\frac{1}{k!\cdot(k+1)}\left(c_k(\tau)-f^{(k)}(\tau)\right)(t-\tau)^{k+1}\right]\right\}\mathrm{d}t
\end{aligned}
\tag{9}
$$

According to Eq. (5), when $c_k(\tau)=f^{(k)}(\tau)$ $(k=1, 2,\ldots, n)$, $S(\tau, f(\tau))$ reaches the maximum value and the time–frequency energy is the most concentrated.

Equation (8) is the expression of nth-order LPFT. When $n=1$ and the c_1 is fixed, the LPFT reduces to LCT. When $n=0$, the LPFT becomes STFT.

Taking signal

$$
s(t) = \sin\left[2\pi\cdot 55\cdot t + 2\pi\cdot\sin(25\cdot t)\right] \tag{10}
$$

as an example, the spectrum of each order LPFT is calculated by using Eq. (8). According to the Ville (1948) formula, the IF of signal (10) can be calculated as

$$
f(t) = 55 + 25\cdot\cos(25\cdot t). \tag{11}
$$

Since Eq. (11) is a continuous derivable function, its derivative expressions can be calculated. For the convenience of expression, only the first to third derivatives are calculated as follows

$$
\begin{aligned}
f^{(1)}(t) &= -25^2\cdot\sin(25\cdot t) \\
f^{(2)}(t) &= -25^3\cdot\cos(25\cdot t) \\
f^{(3)}(t) &= 25^4\cdot\sin(25\cdot t)
\end{aligned}
\tag{12}
$$

The high-concentration time–frequency energy solution of the signal $s(t)$ can be obtained through substituting $f^{(k)}(\tau)$ $(k=1, 2, 3)$ into Eq. (12) by $c_k(\tau)$ $(k=1, 2, 3)$ in Eq. (8), respectively.

Figure 1 shows the signal $s(t)$ (Eq. 10), the IF (Eq. 11) and the results of zeroth–third-order LPFT, which are represented by LPFTk $(k=0, 1, 2, 3)$. In general, the peak position of the time-spectrum energy of each order LPFT, also known as the time–frequency ridges (Gribonval 2001), all concentrate near the IF. However, the energy variation of LPFT0 is too large, which is greatly deviated from the real energy of the signal. Compared to LPFT0, the consistency of the time–frequency energy of other order LPFTs is greatly improved. In Fig. 2, time–frequency ridges and corresponding amplitudes of LPFTs are extracted for IF detection (Terrien et al. 2008). It can be seen in Fig. 2b, the IF errors of LPFT2 and LPFT3 are smaller than LPFT0 and LPFT1. For time–frequency ridge amplitude (Fig. 2c), the variation range of LPFT0 is too large, while the variation range of other LPFTs is small. LPFT3 takes the smallest one, which is consistent with the true amplitude variation trend of the signal.

In order to analyze the concentration of time–frequency energy near the IF of each order LPFT, the index of spectrum concentration (SC) is defined,

$$
\begin{aligned}
&[f_{\min}, f_{\max}] = \arg\underset{f}{}\left\{\mathrm{TFA}(f,t_j) = \frac{\sqrt{2}}{2}\max\left(\mathrm{TFA}(f,t_j)\right)\right\}, \\
&\mathrm{SC}(t_j) = \max\left(\mathrm{TFA}(f,t_j)\right)\Big/\left(f_{\max}-f_{\min}\right)
\end{aligned}
\tag{13}
$$

where TFA represents time–frequency amplitude, $f_{\min}$ and $f_{\max}$ are the lower and upper limits of the frequency analysis, respectively. The first expression in Eq. (13) indicates that

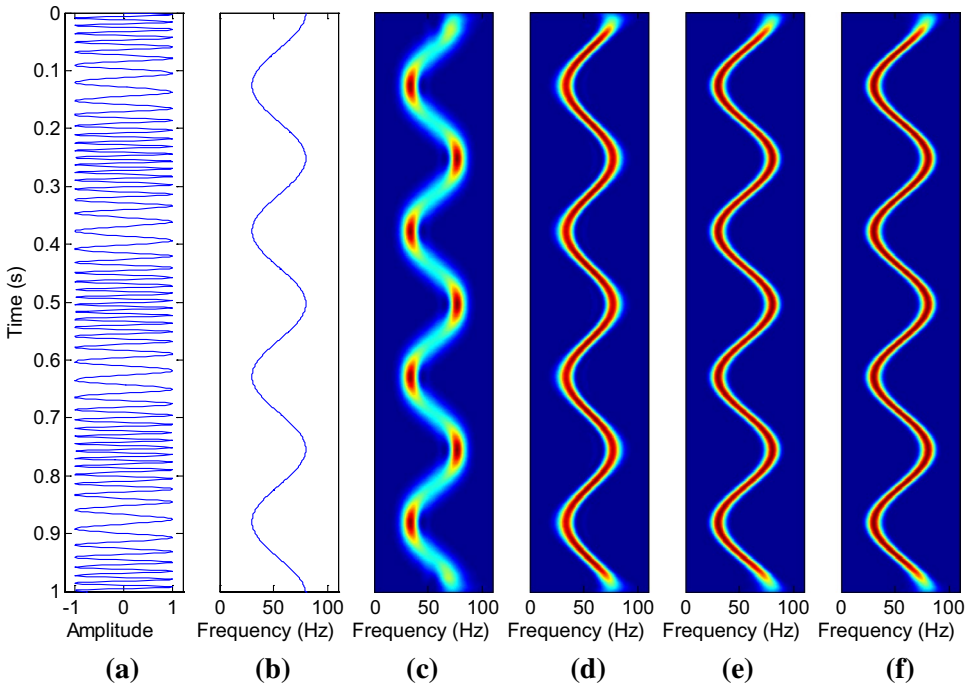

Fig. 1 The zeroth–third-order LPFT with known instantaneous frequencies and derivatives. **a** The signal (10), **b** IF, **c** LPFT0, **d** LPFT1, **e** LPFT2 and **f** LPFT3

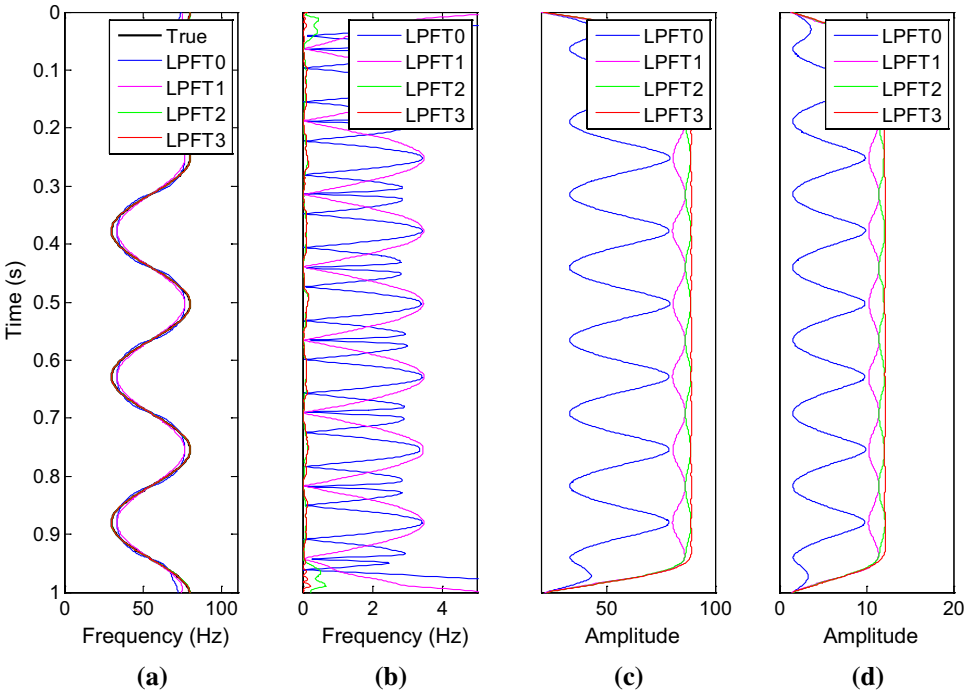

Fig. 2 IF detection and spectral concentration analysis. **a** The true and detection values of IF, **b** IF detection error, **c** time–frequency amplitude at the IF position and **d** spectral concentration of each order LPFT

the values of $f_{\min}$ and $f_{\max}$ are the frequencies corresponding to $\sqrt{2}/2$ of the maxima of TFA.

Based on Eq. (13), when the SC reaches the maximum value, the kernel function of LPFT

$$w(t-\tau)\exp(-i\omega t)\exp\left\{-i\left[\sum_{k=1}^{n}\frac{1}{k!\cdot(k+1)}c_k(\tau)(t-\tau)^{k+1}\right]\right\} \tag{14}$$

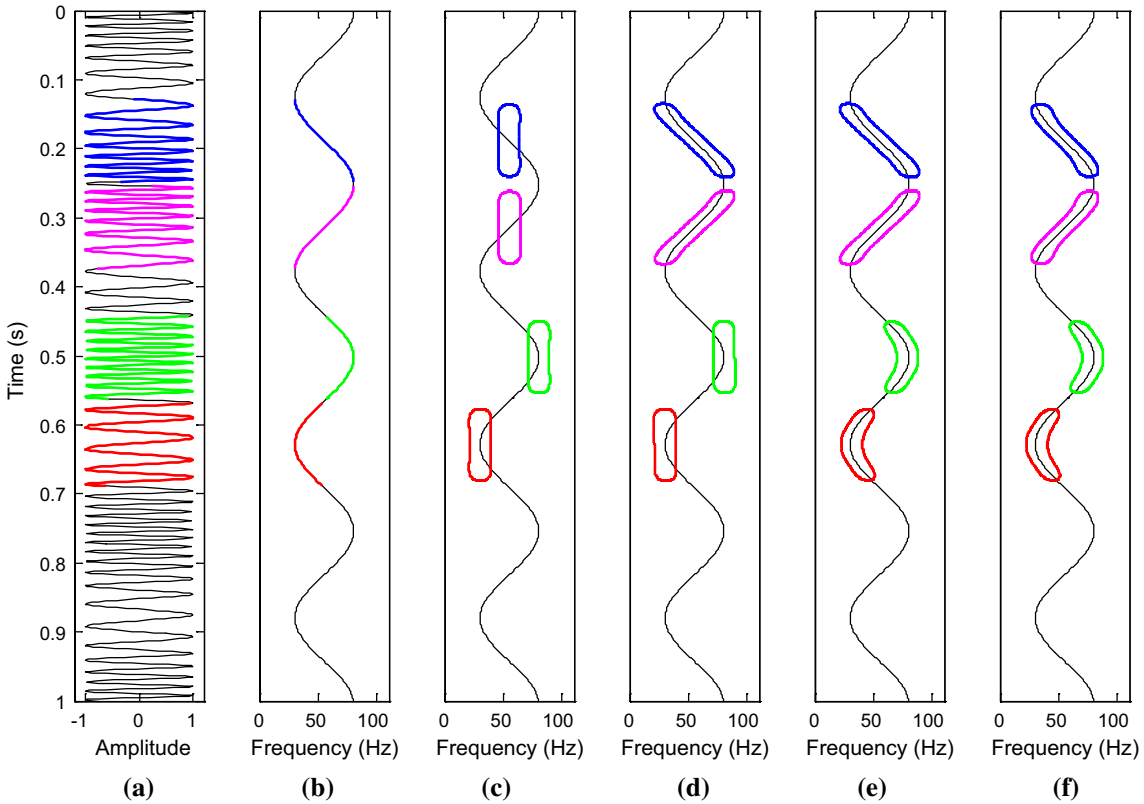

Fig. 3 The correspondence between the spectral shape of the LTFT kernel function and the IF of the signal. **a** Signal, **b** IF, **c** LPFT0, **d** LPFT1, **e** LPFT2 and **f** LPFT3

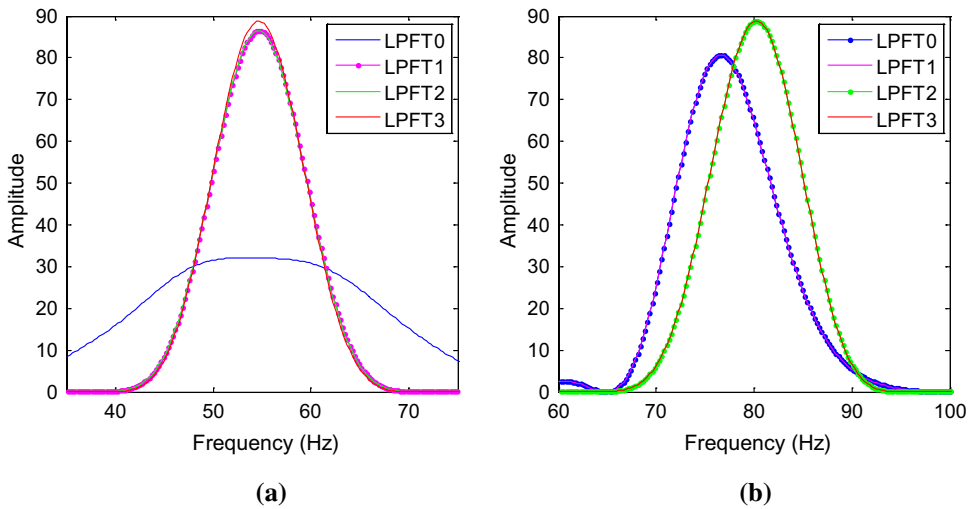

Fig. 4 Spectral amplitude at the typical time **a** 0.188 s and **b** 0.502 s in the time–frequency spectrum of signal (10)

and the frequency variation characteristics of the signal tend to be consistent, and the concentration of the spectrum is the highest. Figure 2d shows the SC of each order LPFT. As the order increases, the spectral concentration of the LPFT is enhanced correspondingly.

For further analysis, the time–frequency spectral contours of the integral of Eq. (14) are calculated targeting the signal (10) with 0.188 s, 0.314 s, 0.502 s, and 0.629 s as the time window centers respectively (Fig. 3). Meanwhile, the spectral amplitudes at 0.188 s and 0.502 s (Fig. 4) are extracted to analyze the properties of the LPFT kernel function.

1. As shown in Fig. 3c, the time–frequency shape of the LPFT0's kernel function is independent of the IF, which

is always parallel to the time or frequency axis. Therefore, when the time–frequency shape of kernel function is more consistent with IF (0.502 s and 0.629 s), the spectral concentration is higher and the time–frequency amplitude is larger (blue dotted line in Fig. 4b). When the time–frequency shape of kernel function is less consistent with IF (0.188 s and 0.314 s), the spectral concentration is lower and the time–frequency amplitude is smaller (blue line in Fig. 4a).

2. For LPFT1 (Fig. 2d), the exponential coefficient of the kernel function is a linear function, so the time–frequency shape can be rotated by a certain angle along the time axis or the frequency axis. Thus for 0.188 s and 0.314 s, the time–frequency spectra of the kernel function are tilted along the direction of the IF. Compared with LPFT0, the spectral concentration and time–frequency amplitude are improved (pink dotted line in Fig. 4a). For 0.502 s and 0.629 s, the time–frequency shapes of the kernel function are similar to that of LPFT0, so the spectral concentration and time–frequency amplitude are close to LPFT0 (pink line in Fig. 4b).
3. For LPFT2 and LPFT3, The exponential coefficients of the kernel function are quadratic and cubic, respectively, so the time–frequency shape can change nonlinearly. For 0.188 s and 0.314 s, the time–frequency shape of LPFT3 is closest to the IF, so its spectral concentration is the highest with the largest time–frequency amplitude (red line in Fig. 4a). The time–frequency shape of LPFT2 is similar to that of LPFT1, so its time–frequency amplitude is also close to that of LPFT1 (green line in Fig. 4a). For 0.502 s and 0.629 s, the time–frequency shapes of LPFT2 and LPFT3 are similar. They all bend with the change of IF, and high degrees of coincidence are obtained. Therefore, the time–frequency amplitudes have reached maximum values, meanwhile the spectrum concentration is the highest (green dotted line and red line in Fig. 4b).

Therefore, under the condition that the coefficients of each order of the polynomial demodulation operator are known in Eq. (7), LPFT can obtain the time–frequency analysis results with a high spectral concentration. For the real signal, it is difficult to obtain the derivatives directly since the IF is unknown. The calculation procedure of nth-order LPFT is designed following the parameter estimation recursive algorithm of Yang et al. 2014:

1. Since LPFT0 does not contain the polynomial demodulation operator, the initial time–frequency spectrum is calculated based on LPFT0 firstly.
2. Detect the time–frequency ridge to obtain the IF $f(t)$.
3. For each time position τ, the derivatives $f^{(k)}(\tau)$ ($k=1, 2, \ldots, n$) are obtained by the least squares method within the time window $w(t-\tau)$ according to Eq. (3).

   Suppose the length of the time window is $2m+1$, Eq. (3) is written in the matrix form

$$\mathbf{A}_{2m\times n}\mathbf{x}_{n\times 1}=\mathbf{b}_{2m\times 1}, \tag{15}$$

   where

$$\mathbf{A}=\begin{bmatrix} (t_{(-m)}-\tau) & \frac{1}{2!}(t_{(-m)}-\tau)^2 & \frac{1}{3!}(t_{(-m)}-\tau)^3 & \cdots & \frac{1}{n!}(t_{(-m)}-\tau)^n \\ \cdots & \cdots & \cdots & \cdots & \cdots \\ (t_{(-1)}-\tau) & \frac{1}{2!}(t_{(-1)}-\tau)^2 & \frac{1}{3!}(t_{(-1)}-\tau)^3 & \cdots & \frac{1}{n!}(t_{(-1)}-\tau)^n \\ (t_{(1)}-\tau) & \frac{1}{2!}(t_{(1)}-\tau)^2 & \frac{1}{3!}(t_{(1)}-\tau)^3 & \cdots & \frac{1}{n!}(t_{(1)}-\tau)^n \\ \cdots & \cdots & \cdots & \cdots & \cdots \\ (t_{(m)}-\tau) & \frac{1}{2!}(t_{(m)}-\tau)^2 & \frac{1}{3!}(t_{(m)}-\tau)^3 & \cdots & \frac{1}{n!}(t_{(m)}-\tau)^n \end{bmatrix},$$

$$\mathbf{x}=\left[f^{(1)}(\tau)\ f^{(2)}(\tau)\ f^{(3)}(\tau)\ \cdots\ f^{(n)}(\tau)\right]^{\mathrm{T}},$$

$$\mathbf{b}=\left[f(t_{(-m)})\ \cdots\ f(t_{(-1)})\ f(t_{(1)})\ \cdots\ f(t_{(m)})\ \right]^{\mathrm{T}}-f(\tau).$$

   The solution of Eq. (15) is

$$\mathbf{x}=\left(\mathbf{A}^{\mathrm{T}}\mathbf{A}+\lambda\mathbf{I}\right)^{-1}\mathbf{A}^{\mathrm{T}}\mathbf{b}, \tag{16}$$

   where λ is the damping factor, and $\mathbf{I}$ is unit matrix.
4. Let $c_k(\tau)=f^{(k)}(\tau)$ ($k=1, 2,\ldots, n$), calculate the LPFTn of the signal based on Eq. (8).
5. Return to step 2, the IF $f(t)$ is calculated cyclically. The termination condition lies in reaching the maximum iterations or the error of two adjacent IF is less than a preset threshold.
6. Output the LPFTn satisfying the iteration termination condition.

Based on the flow mentioned above, the first–third-order LPFT time–frequency spectra of the signal (10) are computed and compared with the results of LCT and GLCT (Fig. 5). For convenience of comparison, two time–frequency tilt angles of $\pi/8$ (Fig. 5a) and $-\pi/8$ (Fig. 5b) are chosen for LCT, respectively. As the time–frequency slope in each LCT remains unchanged, the amplitude performance is either high or low, showing an intensive inconsistency and deviation from the real time–frequency amplitude of the signal. By changing the time–frequency slope in each local time–frequency point, GLCT improves the accuracy of time–frequency amplitude (Fig. 5c). Figure 5d–f is the time–frequency spectra of the first–third-order LPFT, respectively. As the order increases, the consistency and accuracy of the time–frequency amplitude step forward.

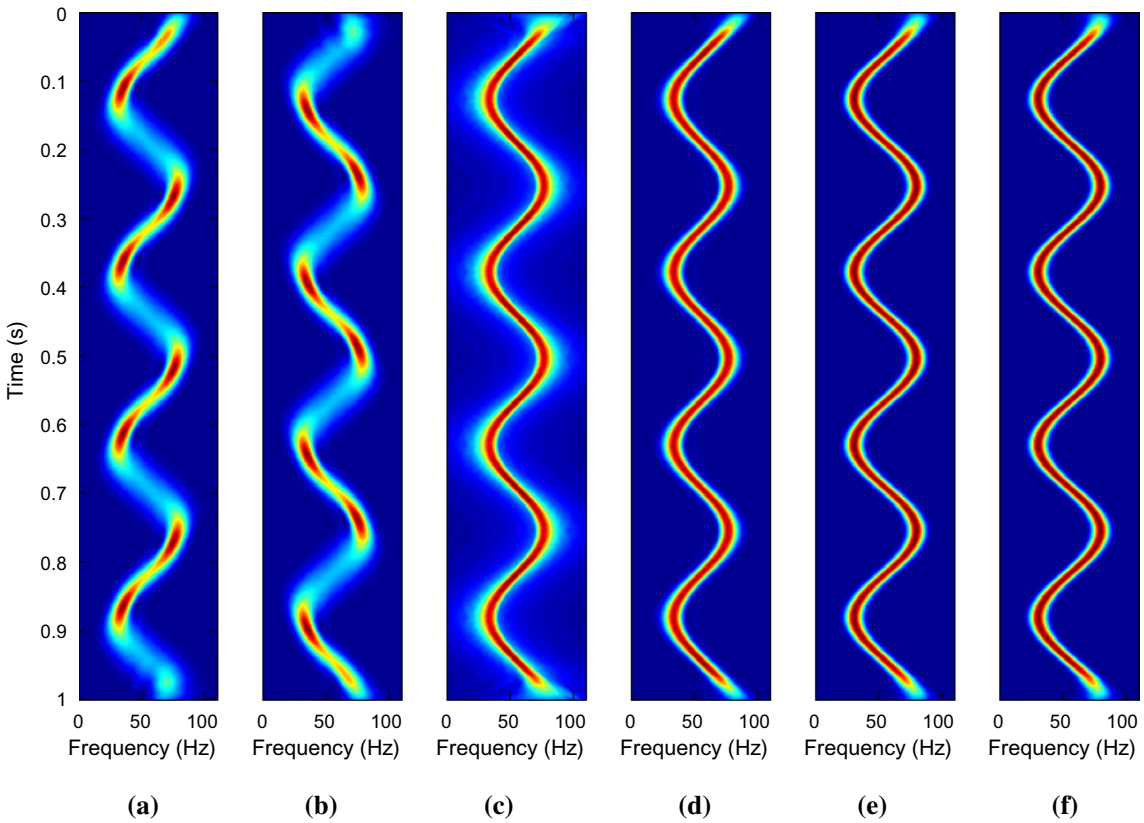

Fig. 5 Time–frequency spectra of LCT with time–frequency tilt angle of **a** $\pi/8$ and **b** $-\pi/8$, **c** GLCT, **d** LPFT1, **e** LPFT2 and **f** LPFT3

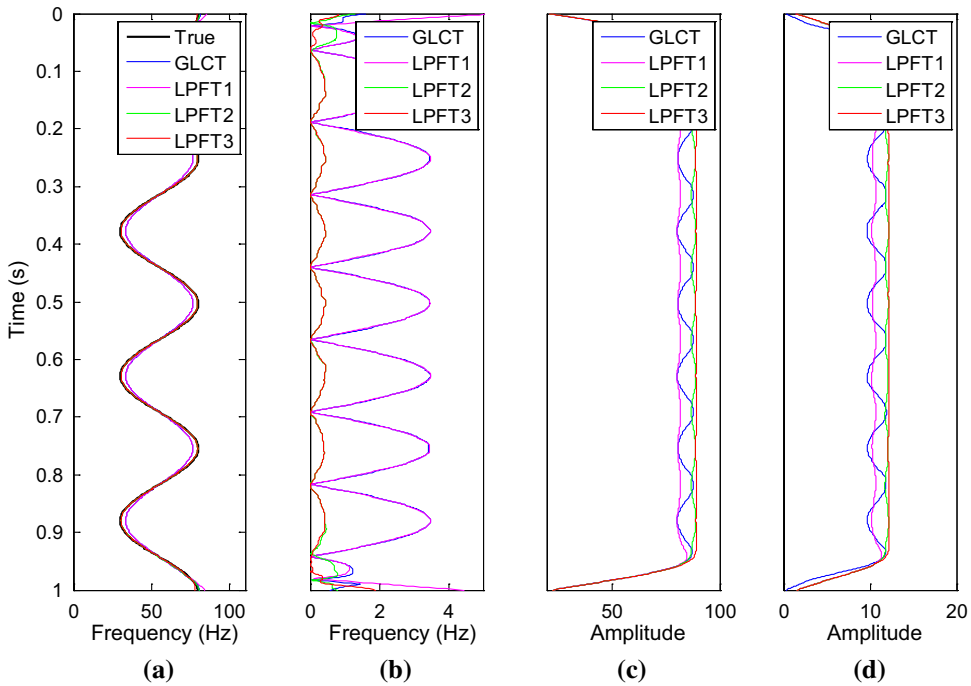

Fig. 6 IF detection and spectral concentration analysis. **a** The true and detection values of IF, **b** IF detection error, **c** time–frequency amplitude at the IF position, and **d** spectral concentration of GLCT and first–third-order LPFT

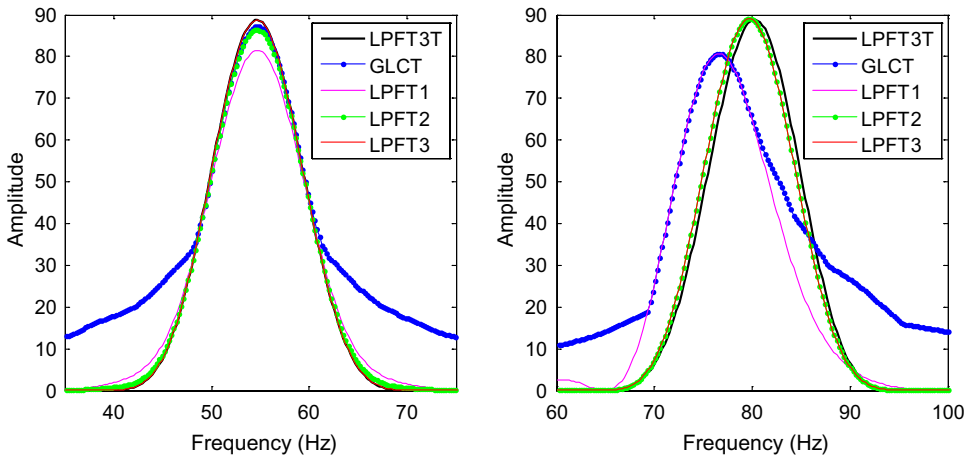

Fig. 7 Spectral amplitude at the typical time **a** 0.188 s and **b** 0.502 s in the time–frequency spectrum of signal (10)

Figure 6 shows the results of IF detection and spectral concentration analysis about the four methods of GLCT, LPFT1, LPFT2 and LPFT3 in Fig. 5. It can be seen from the IF detection errors (Fig. 6b), since both GLCT and LPFT1 belong to the first-order fitting of the local time–frequency characteristics of the signal, the error values have the same magnitude. LPFT2 and LPFT3 reduce the IF errors by the high-order fitting of the local time–frequency characteristics. Comparative analysis of time–frequency spectra (Fig. 6c) shows LPFT3 has the largest amplitude. Furthermore, the SC of the four time–frequency spectra are calculated based on Eq. (13). Figure 6d shows that LPFT3 has the highest spectral concentration.

For further analysis, the spectral amplitudes of GLCT and first–third-order LPFT at time 0.188 s and 0.502 s are extracted (Fig. 7). Compared with the third-order LPFT based on the true IF derivatives (Fig. 1) which is represented by LPFT3T here, it can be seen that the result of GLCT deviates the farthest from LPFT3T. Compared with GLCT, the accuracy of each order LPFT is improved. The higher the order, the more obvious the improvement of the accuracy.

Examples

The synthetic traces are generated by using chirplet and Ricker wavelet with different IF characteristics, respectively. The LPFT of the traces are obtained. Considering the variation of magnitude in the IF, only the third order is calculated. It is also compared with the traditional time–frequency analysis methods in seismic exploration, which are STFT, CWT, ST, and the MP method based on the Ricker atomic dictionary (Liu and Marfurt 2007).

Figure 8a shows the synthetic trace with chirplet, IF and its time–frequency spectrum by STFT, CWT, ST, MP and LPFT, respectively. The five chirplets are generated by the formula

$$w(t) = \cos\left\{2\pi\left[\omega_1(t-\tau_1) + \omega_2(t-\tau_2)^2 + \omega_3(t-\tau_3)^3 + \omega_4(t-\tau_4)^4\right]\right\} \tag{17}$$

multiplied with a Gaussian window. The parameters of each chirplet are shown in Table 1.

Among the five chirplets, the IF of the first one changes linearly; the 2nd, 3rd and 4th are nonlinear; and the 5th is constant. For STFT, CWT and ST, the time–frequency morphology reflects the IF variation of each wavelet to a certain extent, but the spectral magnitude shows a large difference, especially for ST. This is due to the quasi-stationary assumptions of these methods. When the IF does not change in the time window, such as the fifth chirplet, the local signal conforms to the stationary characteristic. The perfect fitting of the signal can be obtained based on the orthogonal time–frequency grid, so the time–frequency shape and amplitude of the signal are well preserved. However, when the IF changes in the time window, such as the first–fourth chirplets, the local signal does not conform to the stationary features. The orthogonal time–frequency grid can only achieve an approximate fitting of the IF, which inevitably undermines the time–frequency variation and thus damages the time–frequency amplitude. For the MP method, the signal-based instantaneous autocorrelation transform can well preserve the time–frequency energy and have a higher time–frequency resolution. However, its time–frequency shape is difficult to reflect the variation characteristics of the IF. This is because the frequency-related parameters in the atomic dictionary only reflect the central frequency of the local signal and fail to reflect the frequency variation characteristics in the local time period. For LPFT, the polynomial demodulation operator can fit the IF effectively. Thus, the time–frequency shape can accurately reflect the IF variation characteristics, and the time–frequency energy of the signal can also be well preserved.

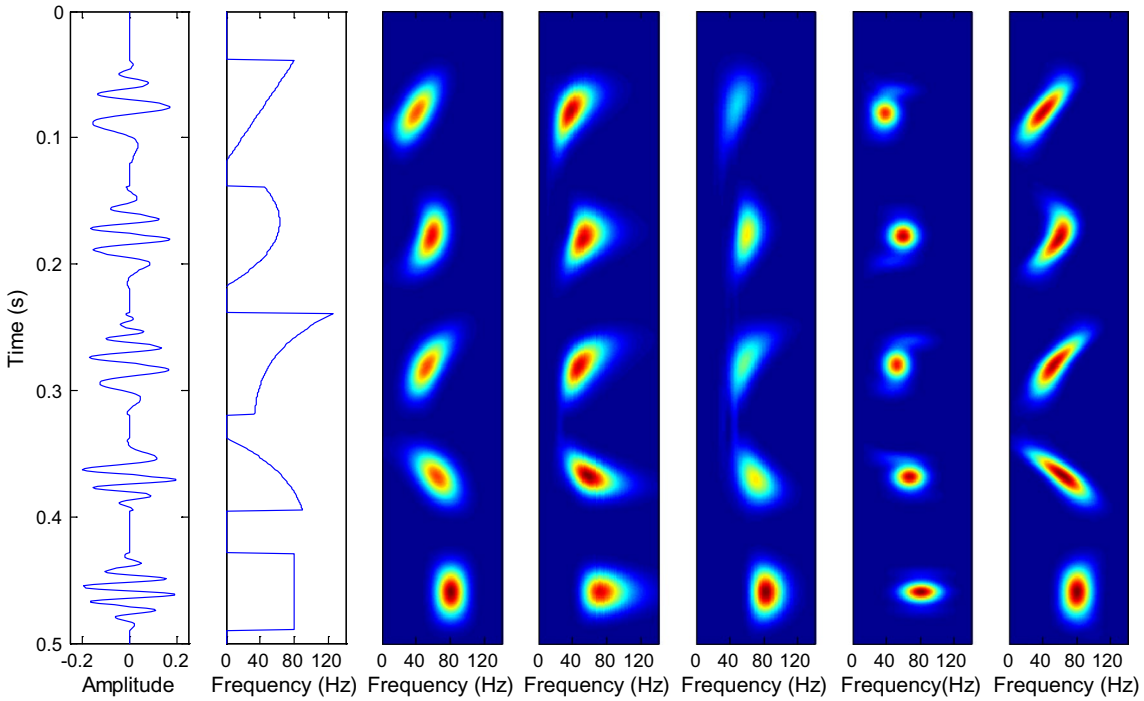

(a)

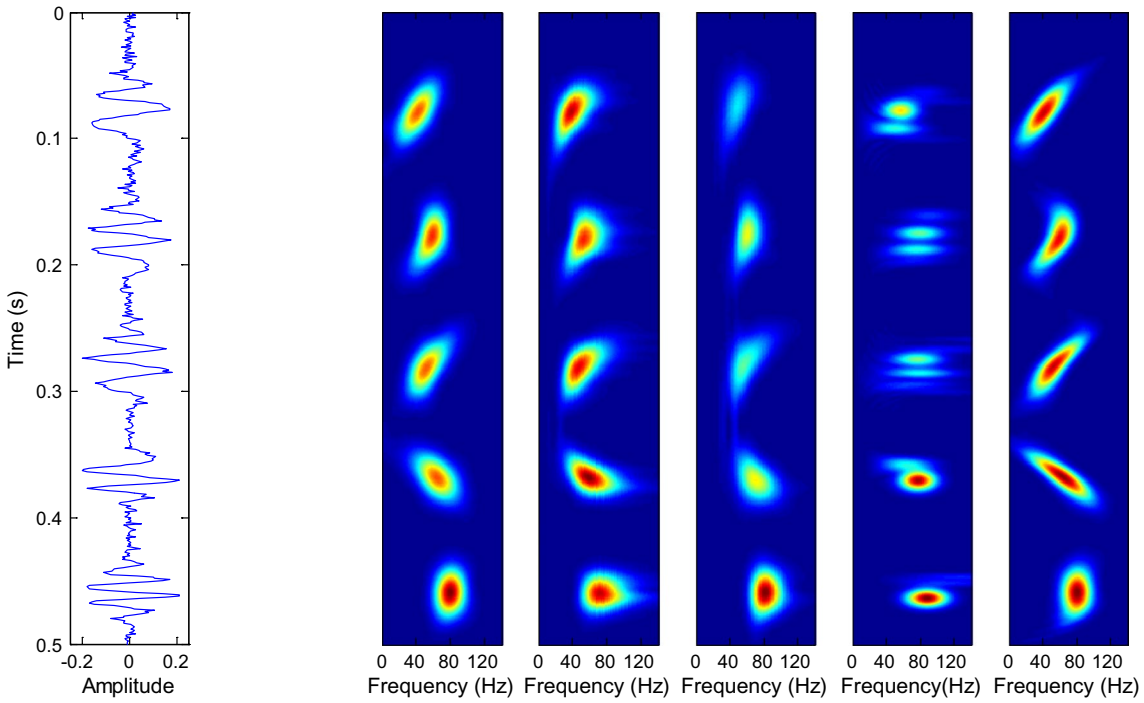

(b)

Fig. 8 Synthetic trace with chirplet and time–frequency spectra analysis. **a** Time–frequency spectra of noise-free data, from left to right, they are synthetic trace, IF, and the spectra by STFT, CWT, ST, MP and LPFT, respectively. **b**, **c** Time–frequency spectra with 5% and 10% noise, respectively, where the subgraphs have the same meaning as **a**

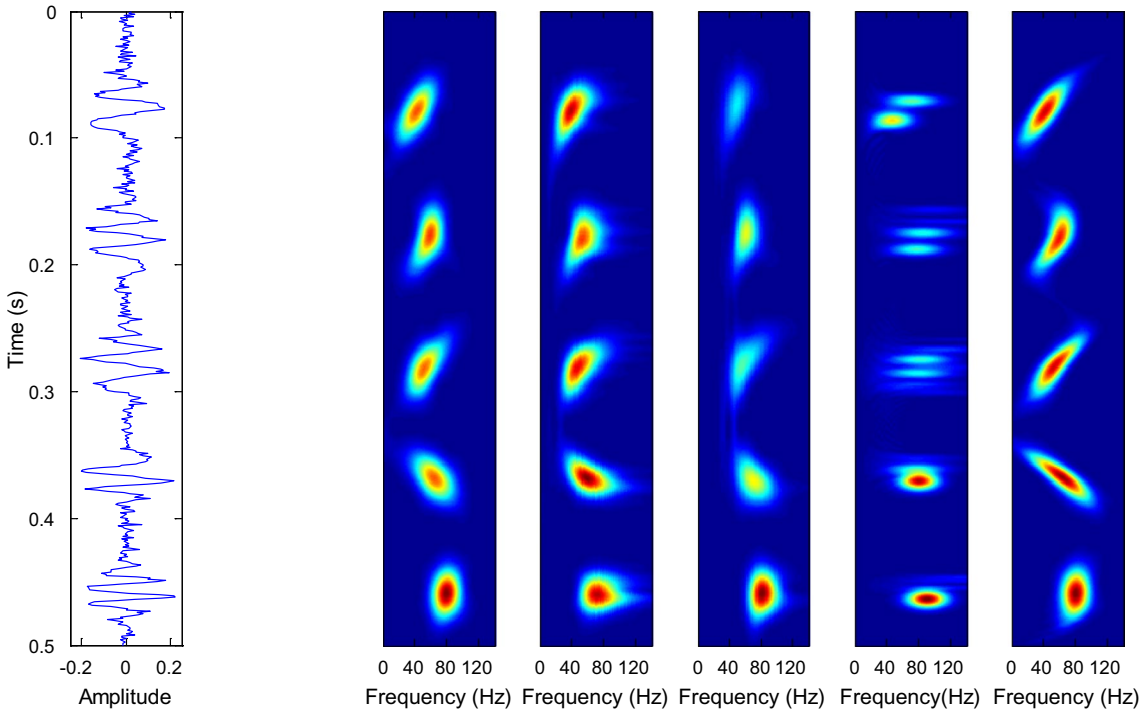

(c)

Fig. 8 (continued)

Table 1 The parameters of each chirplet in Fig. 8a

Number	ω_1 (Hz)	τ_1 (s)	ω_2 (Hz)	τ_2 (s)	ω_3 (Hz)	τ_3 (s)	ω_4 (Hz)	τ_4 (s)
1	30	0	500	0.05	0	0	0	0
2	50	0	300	0.055	8000	0.04	0	0
3	30	0	100	0.1	1500	0.1	30,000	0.1
4	100	0.028	100	0.1	1500	0.1	30,000	0.1
5	80	0.02	0	0	0	0	0	0

Figure 8b, c shows the time–frequency spectrum of different methods after adding, respectively, 5% and 10% random noise to the synthetic signal (Fig. 8a). It can be seen from the results that these methods all have anti-noise ability to a certain extent. Among the five methods, the deteriorated result of MP is mainly caused by the imperfect match between the atomic dictionary and signal.

Similar to Figs. 8a and 9a is a synthetic trace associated with the Ricker wavelet. With the increase of time, the wavelet is gradually changed from symmetrical to asymmetrical, and the IF gradually appears tailing, which corresponds to the dispersion in the process of seismic wave propagation (Wang 2004). The time–frequency energy characteristics of each wavelet are well preserved in five time–frequency spectrum results. However, compared with STFT, CWT, ST and MP, the time–frequency morphology of LPFT reflects the IF variation characteristics of each wavelet more accurately. Therefore, LPFT has the advantage of retaining both time–frequency morphological features and energy features. The anti-noise capability of these methods shows up in the results of noisy synthetic trace (Fig. 9b, c). In addition, compared to Fig. 8b, c, the anti-noise ability of the MP method has been improved due to the perfect match of the time–frequency dictionary and the signal.

To further verify the ability of the proposed method, the interlayer velocity model is designed in Fig. 10. The model is divided into three groups from top to bottom, and the thickness of the interbed layer is gradually thinned. Synthetic trace

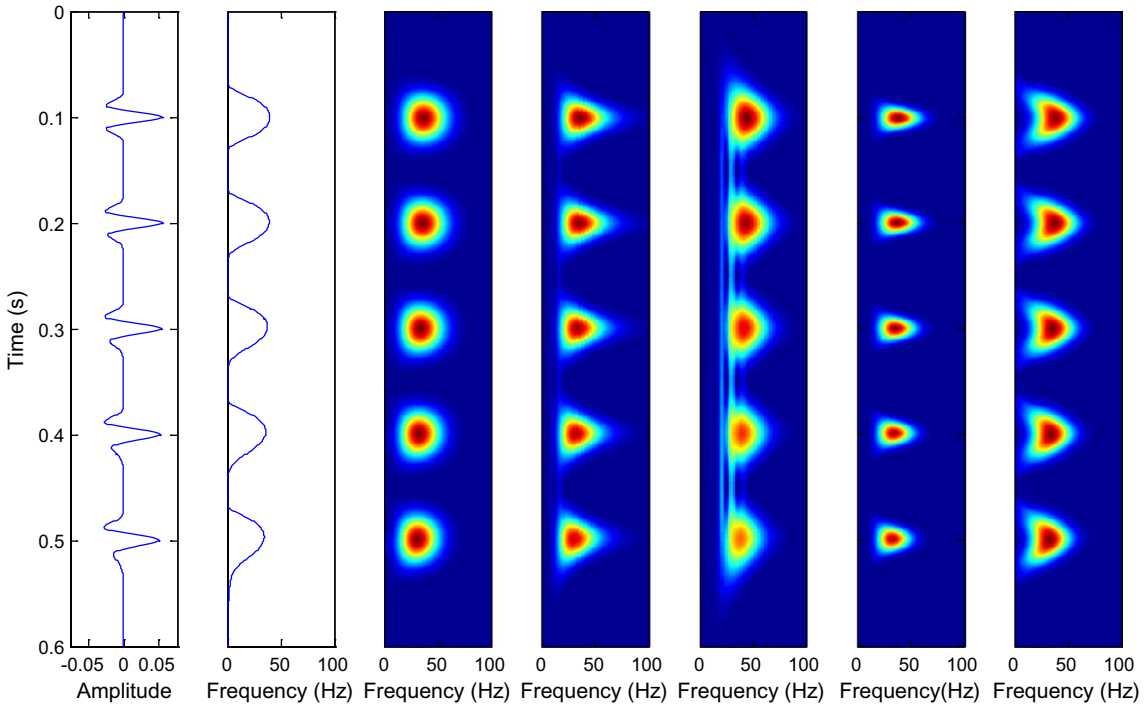

(a)

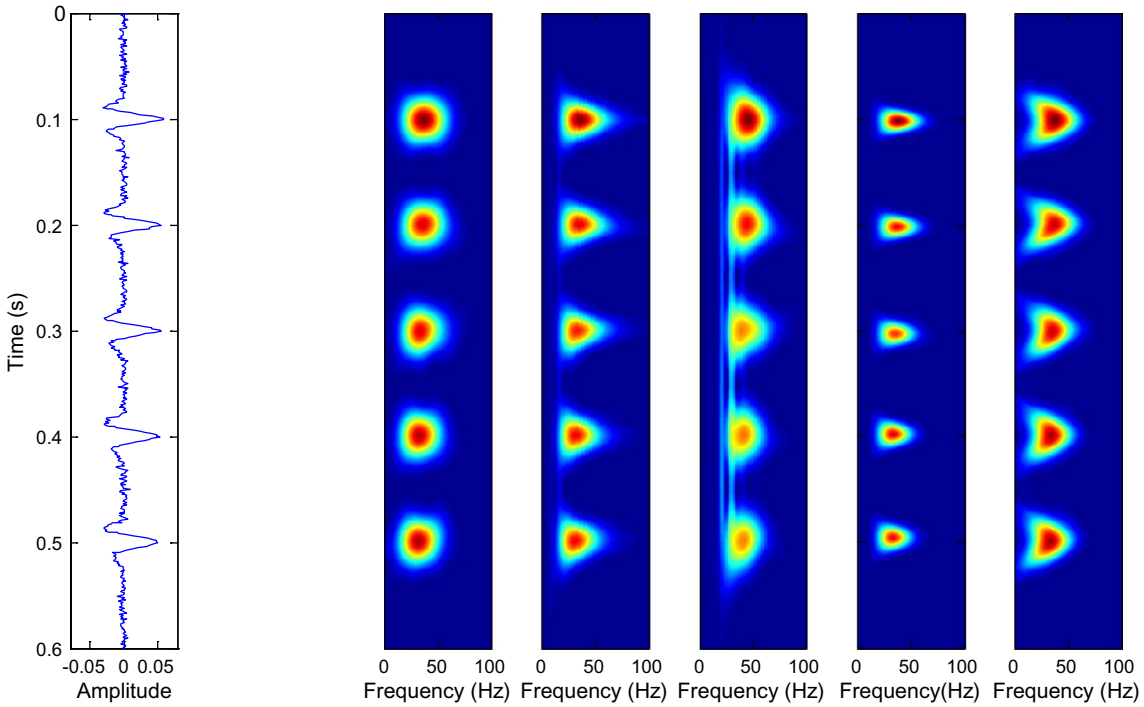

(b)

Fig. 9 Synthetic trace with Ricker wavelet and time–frequency spectra analysis. **a** Time–frequency spectra of noise-free data, from left to right, they are synthetic trace, IF, and the spectra by STFT, CWT, ST, MP and LPFT, respectively. **b**, **c** Time–frequency spectra with 5% and 10% noise, respectively, where the subgraphs have the same meaning as **a**

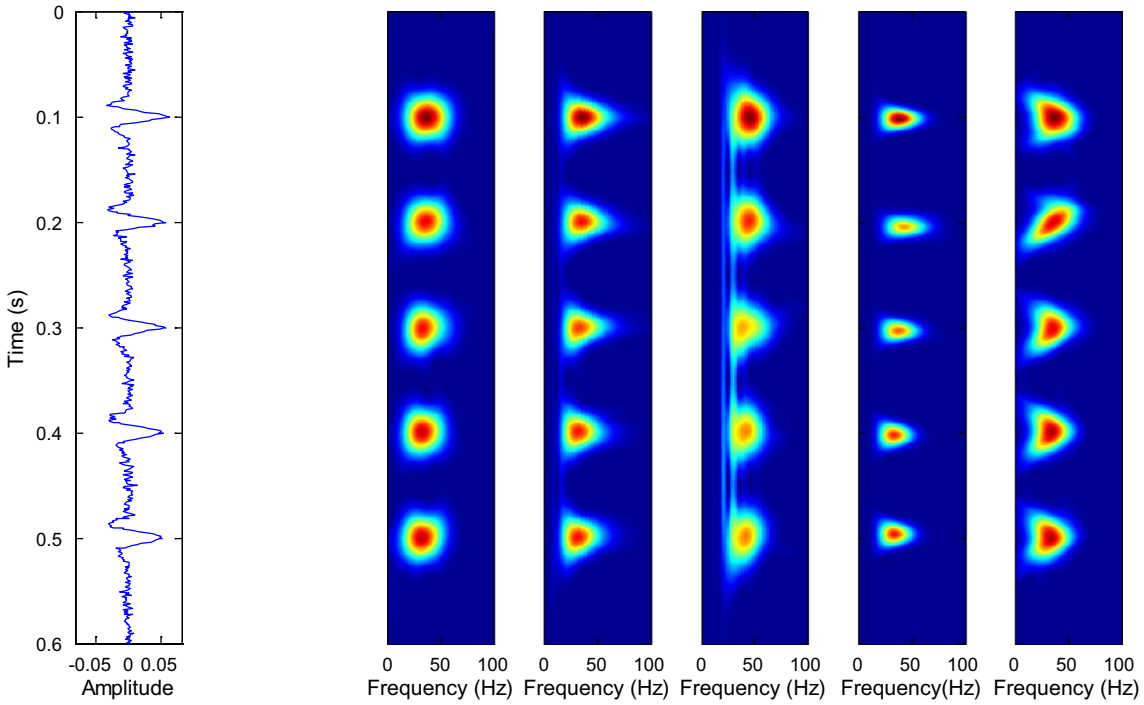

(c)

Fig. 9 (continued)

and IF curve are obtained based on the zero-phase Ricker wavelet (Fig. 11). For the first group of the interlayers, the IF curve changes slightly. STFT, CWT, MP and LPFT maintain the IF variation characteristics and energy relationship. For the second group of the interlayers, the IF shows wavy characteristics. STFT, CWT, ST and MP are all unable to describe the change, while only LPFT3 can retain the IF variation feature well. For the third group, the IF exhibits an arc-like feature. STFT, CWT, ST, and LPFT can all describe this time–frequency morphology, and the morphological variation of the LPFT spectrum is closest to the IF.

Since LPFT is a high-order form of STFT, the computational cost of LPFT is greater than that of STFT. For a more comprehensive comparison, the time consumption of different TFA methods in the three examples (Figs. 8, 9, 10) was recorded. The CPU of the tested computer is Intel Xeon 5 2.8 GHz, and the RAM is 16 GB. It can be seen from Table 2 that, among the five methods, STFT and ST take less time, CWT takes moderate time, and MP and LPFT take more time.

Applications

Figure 12 shows a two-dimensional post-stack seismic profile that has undergone the conventional processing such as static correction, denoising, deconvolution, migration and stacking. The seismic reflection characteristics of typical fluvial facies strata are displayed between 2.9 and 3.1 s, that is, short axial strong reflection in the overall weak reflection background. The weak reflection mainly reflects the mudstone background, while the strong reflection is usually the response of channel sandstone. The three events marked in the elliptic region in Fig. 12 have already been proved to be the response of three thin channel sandstones stacked vertically. The planar distribution characteristics of the three channel sandstones are shown in Fig. 13. The representative seismic traces of the channel sandstones (trace number 95) and the mudstone background (trace number 170) are extracted, and the corresponding time–frequency spectra are calculated.

Figure 14 shows the time–frequency spectra of the seismic trace at the channel sandstones. On the whole, the channel sand bodies between 2.9 and 3.1 s have strong time–frequency energy. By comparison, note that CWT and ST cannot distinguish the response of the three sand bodies well. Although STFT distinguishes the three sand bodies, typical low-frequency oscillations occur in the time–frequency spectrum due to the short-time window (Castagna et al. 2003). MP shows a high resolution, and the response of the three sand bodies are all labeled as independent energy

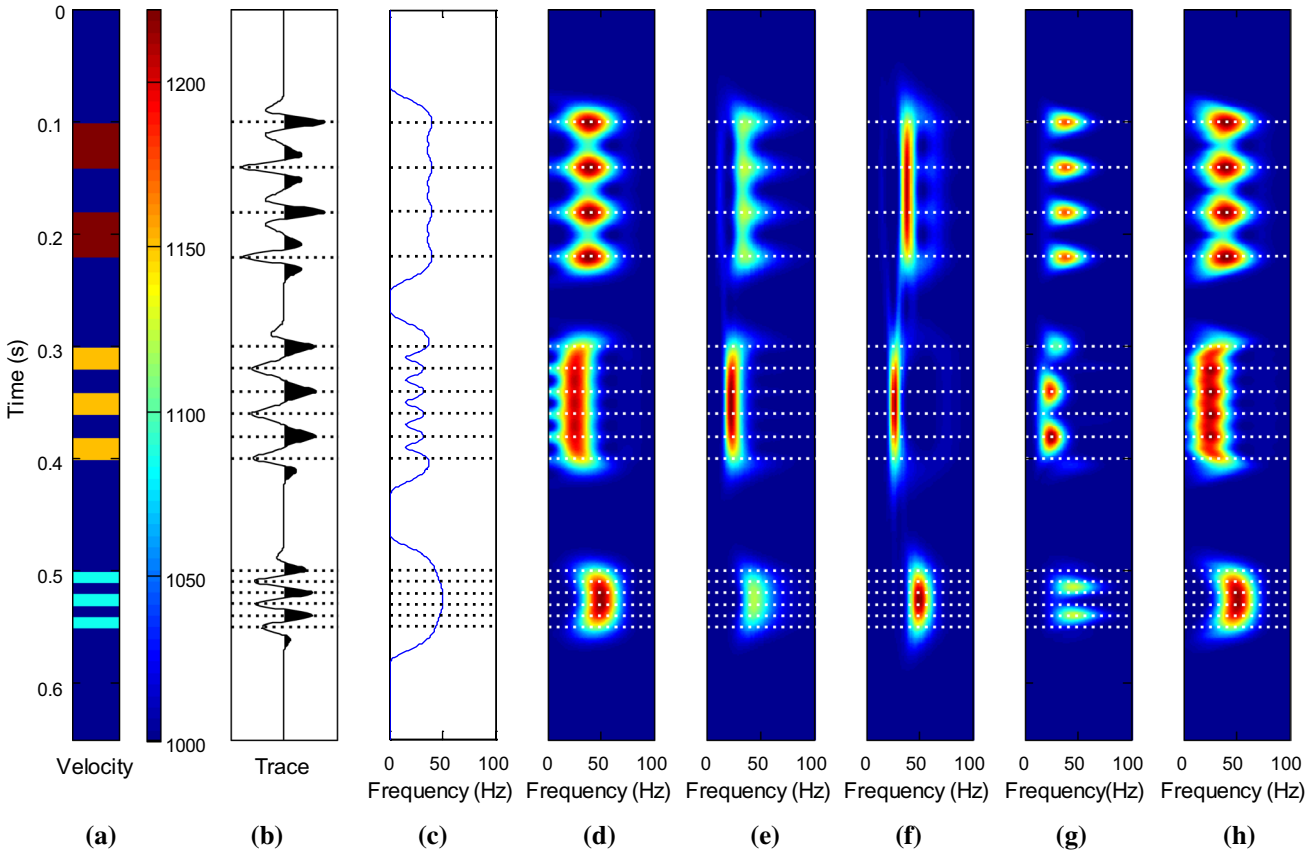

Fig. 10 Time–frequency spectra analysis of seismic trace with interbedded model. From left to right, they are **a** velocity model, **b** synthetic trace, **c** IF and time–frequency spectrum by **d** STFT, **e** CWT, **f** ST, **g** MP and **h** LPFT, respectively

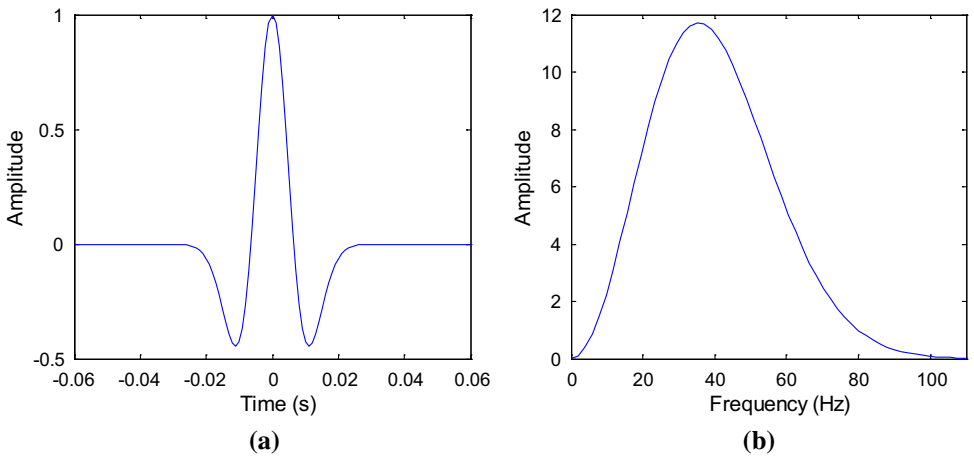

Fig. 11 Ricker wavelet (**a**) and the amplitude spectrum (**b**)

Table 2 The cost time of different TFA methods on the three traces in Figs. 8, 9 and 10

Synthetic trace	STFT (s)	CWT (s)	ST (s)	MP (s)	LPFT (s)
Chirplet	0.12	0.25	0.09	0.32	0.39
Rikcer	0.14	0.29	0.11	0.41	0.48
Interbed	0.17	0.42	0.15	0.58	0.64

clusters. However, the shapes are similar, the local frequency variation characteristics of each waveform cannot be delineated. LPFT not only discerns the three sand bodies, but also depicts the local frequency variation characteristics.

Figure 15 shows the time–frequency spectra of the seismic trace at the mudstone background. Since the seismic reflection between the target layers is weak, the corresponding

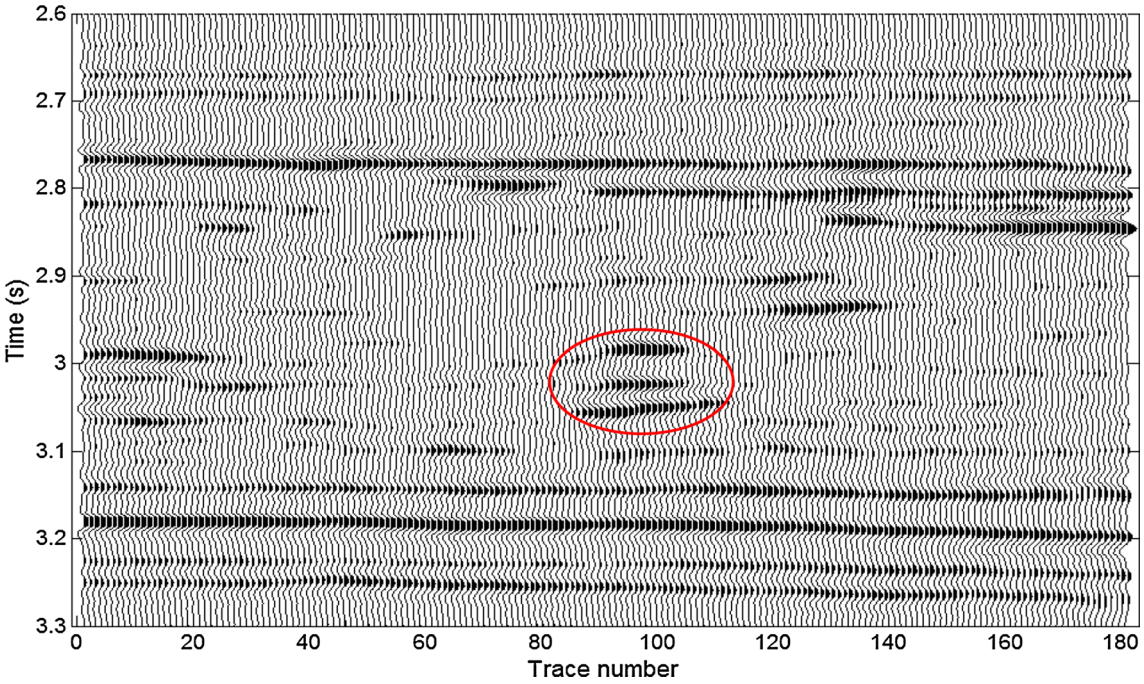

Fig. 12 Real seismic data. The events marked by the elliptic are the response of three channel sandstones

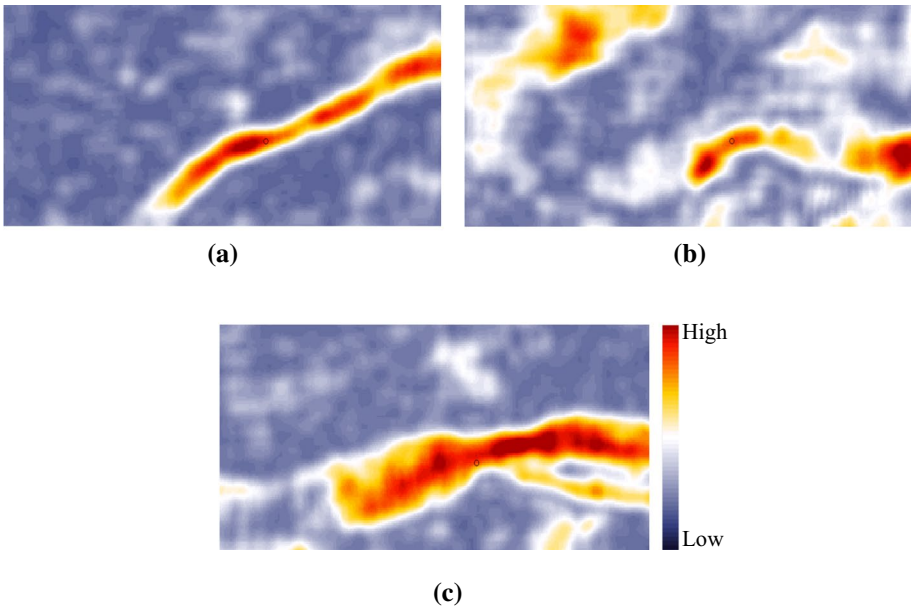

Fig. 13 Planar distribution characteristics of the three channel sandstones in Fig. 12 based on amplitude attribute. The position of the black circle corresponds to the 95th trace in Fig. 12

time–frequency energy is also feeble. However, outside the target layer, from the time–frequency spectrum of strongly reflected waveform at 2.8 s, it can be seen that MP and LPFT have a high resolution. For the time–frequency spectrum of strongly reflected waveform at 3.2 s, LPFT well retains the IF variation characteristics of seismic waves.

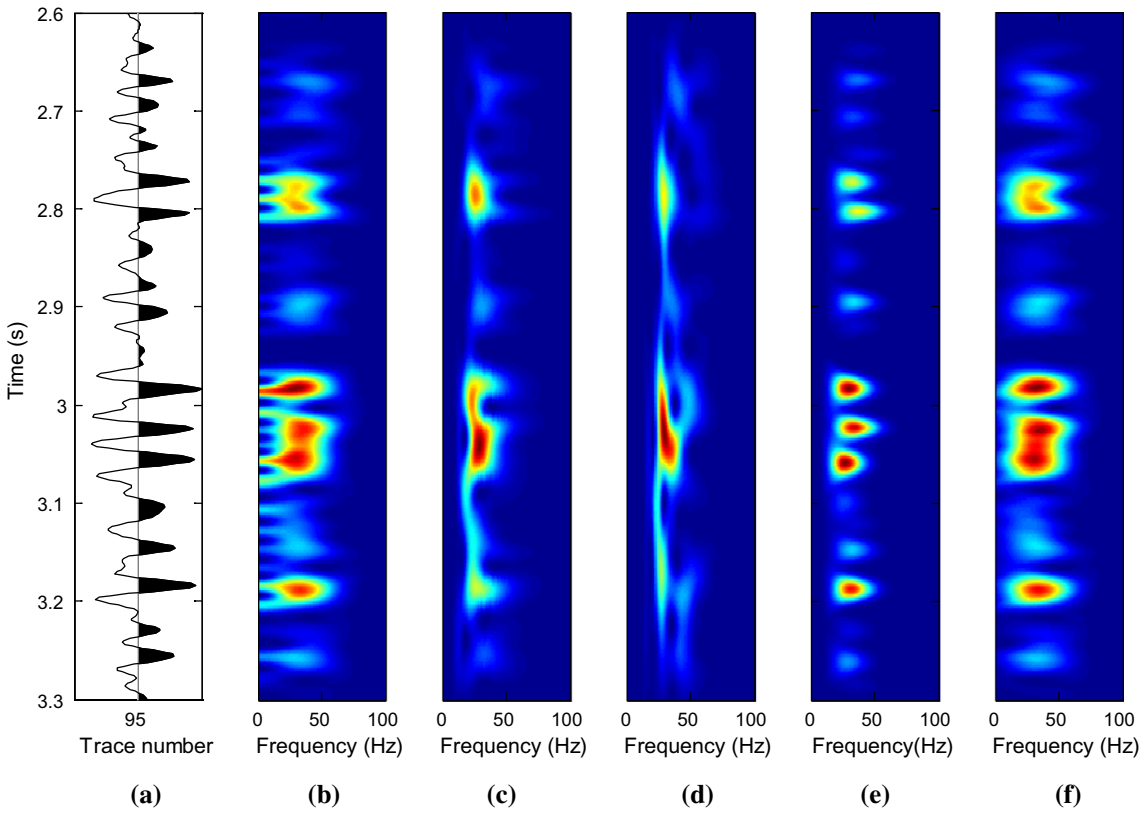

Fig. 14 Time–frequency spectrum analysis of seismic trace at the location of channel sandstones. From left to right, they are **a** seismic trace, and time–frequency spectrum by **b** STFT, **c** CWT, **d** ST, **e** MP and **f** LPFT, respectively

Conclusions

The LPFT method based on the Ville's analytical signal shows that LPFT is a higher order form of STFT and LCT. Through the polynomial demodulation operator, LPFT can achieve high-order fitting of local time–frequency features of the signal through accurate determination of the demodulation operator coefficients. The calculation process of LPFT given in this paper can solve the demodulation operator coefficients, and then obtain the time–frequency spectrum results with high energy concentration.

For non-stationary seismic traces, LPFT not only exhibits high time–frequency resolution, but also effectively preserves the instantaneous frequency and amplitude variation characteristics of local seismic signals. These properties can be utilized for target detection with frequency and amplitude anomalies, for example, in gas-bearing reservoirs with dispersion and attenuation characteristics. LPFT can be applied to prestack gathers, with which the prestack prediction of gas-bearing reservoirs can be realized by using the varied characteristics of frequency with offset. In addition, LPFT can be combined with spectral decomposition technology to realize the post-stack prediction of gas-bearing reservoirs related to low-frequency shadow phenomenon. These potential research will be carried out in the future.

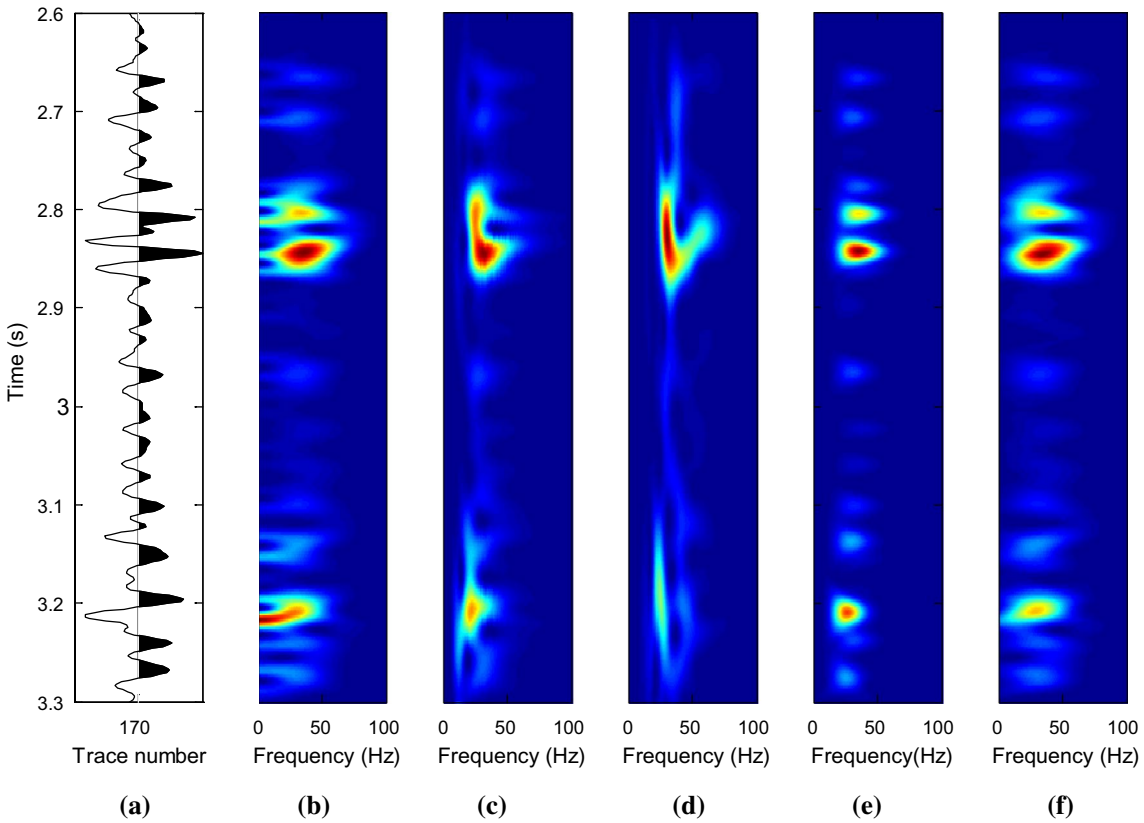

Fig. 15 Time–frequency spectrum analysis of seismic trace at the location of the mudstone background. From left to right, they are **a** seismic trace, and time–frequency spectrum by **b** STFT, **c** CWT, **d** ST, **e** MP and **f** LPFT, respectively

Acknowledgements This work was financially supported by the National Science and Technology Major Project of China (2016ZX05003-003) and Inversion Methods Study of Sedimentary Model Constrained Lithofacies and Fluid Identification (P18075-6).

References

Castagna JP, Sun SJ, Siegfried RW (2003) Instantaneous spectral analysis: detection of low-frequency shadows associated with hydrocarbons. Lead Edge 22(2):120–127

Cohen L (1995) Time–frequency analysis. Prentice Hall, Upper Saddle River

Durak L, Arikan O (2003) Short-time Fourier transform: two fundamental properties and an optimal implementation. IEEE Trans Signal Process 51(5):1231–1242

Gribonval R (2001) Fast matching pursuit with a multiscale dictionary of Gaussian chirps. IEEE Trans Signal Process 49(5):994–1001

Kadambe S, Boudreaux-Bartels GF (1992) A comparison of the existence of 'cross terms' in the Wigner distribution and the squared magnitude of the wavelet transform and the short-time Fourier transform. IEEE Trans Signal Process 40(10):2498–2517

Katkovnik V (1998) Discrete-time local polynomial approximation of the instantaneous frequency. IEEE Trans Signal Process 46(10):2626–2637

Li X, Bi G, Stankovic S, Zoubir AM (2011) Local polynomial Fourier transform: a review on recent developments and applications. Signal Process 91(6):1370–1393

Li D, Castagna JP, Goloshubin G (2016) Investigation of generalized S-transform analysis windows for time–frequency analysis of seismic reflection data. Geophysics 81(3):V235–V247

Liu J, Marfurt KJ (2007) Instantaneous spectral attributes to detect channels. Geophysics 72(2):P23–P31

Liu NH, Gao JH, Jiang XD, Zhang ZS, Wang Q (2016) Seismic time–frequency analysis via STFT-based concentration of frequency and time. IEEE Geosci Remote Sens Lett 14(1):127–131

Mallat SG, Zhang Z (1993) Matching pursuits with time–frequency dictionaries. IEEE Trans Signal Process 41(12):3397–3415

Mann S, Haykin S (1995) The chirplet transform: physical considerations. IEEE Trans Signal Process 43(11):2745–2761

Naseer MT, Asim S (2017) Detection of cretaceous incised-valley shale for resource play, Miano gas field, SW Pakistan: spectral decomposition using continuous wavelet transform. J Asian Earth Sci 147:358–377

Ouadfeul SA, Aliouane L (2014) Random seismic noise attenuation data using the discrete and the continuous wavelet transforms. Arab J Geosci 7(7):2531–2537

Parolai S (2009) Denoising of seismograms using the S transform. Bull Seismol Soc Am 99(1):226–234

Partyka G, Gridley J, Lopez J (1999) Interpretational applications of spectral decomposition in reservoir characterization. Lead Edge 18(3):353–360

Phinyomark A, Limsakul C, Phukpattaranont P (2011) Application of wavelet analysis in EMG feature extraction for pattern classification. Meas Sci Rev 11(2):45–52

Puryear CI, Portniaguine ON, Cobos CM, Castagna JP (2012) Constrained least-squares spectral analysis: application to seismic data. Geophysics 77(5):V143–V167

Radad M, Gholami A, Siahkoohi HR (2015) S-transform with maximum energy concentration: application to non-stationary seismic deconvolution. J Appl Geophys 100(118):155–166

Rene RM, Fitter JL, Forsyth PM, Kim KY, Murray DJ, Walters JK, Westerman JD (1986) Multicomponent seismic studies using complex trace analysis. Geophysics 51(6):1235–1251

Sinha S, Routh P, Anno P (2009) Instantaneous spectral attributes using scales in continuous-wavelet transform. Geophysics 74(2):WA137–WA142

Smith M, Perry G, Stein J, Bertrand A, Yu G (2008) Extending seismic bandwidth using the continuous wavelet transform. First Break 26(6):97–102

Sun S, Castagna JP, Siegfried RW (2002) Examples of wavelet transform time–frequency analysis in direct hydrocarbon detection. In: SEG technical program expanded abstracts, pp 457–460

Terrien J, Marque C, Germain G (2008) Ridge extraction from the time–frequency representation (TFR) of signals based on an image processing approach: application to the analysis of uterine electromyogram AR TFR. IEEE Trans Biomed Eng 55(5):1496–1503

Ville J (1948) Theorie et application de la notion de signal analytic. Cables Transm 93:61–74

Wang YH (2004) *Q* analysis on reflection seismic data. Geophys Res Lett 31:L17606

Wang YH (2006) Inverse *Q*-filter for seismic resolution enhancement. Geophysics 71(3):V51–V60

Wang YH (2010) Multichannel matching pursuit for seismic trace decomposition. Geophysics 75(4):V61–V66

Wang LL, Gao JH, Zhao W, Jiang XD (2012) Enhancing resolution of nonstationary seismic data by molecular-gabor transform. Geophysics 78(1):V31–V41

Wang TY, Yuan SY, Gao JH, Li SJ, Wang SX (2019) Multispectral phase-based geosteering coherence attributes for deep stratigraphic feature characterization. IEEE Geosci Remote Sens Lett 16(8):1309–1313

Wu L, Castagna JP (2017) S-transform and Fourier transform frequency spectra of broadband seismic signals. Geophysics 82(5):O71–O81

Yang Y, Peng ZK, Dong XJ, Zhang WM, Meng G (2014) General parameterized time–frequency transform. IEEE Trans Signal Process 62(11):2751–2764

Yu G, Zhou YQ (2016) General linear chirplet transform. Mech Syst Signal Process 70:958–973

Yuan SY, Wang SX, Ma M, Ji YZ, Deng L (2017) Sparse Bayesian learning-based time-variant deconvolution. IEEE Trans Geosci Remote Sens 55(11):6182–6194

Yuan SY, Ji YZ, Shi PD, Zeng J, Gao JH, Wang SX (2019a) Sparse Bayesian learning-based seismic high-resolution time–frequency analysis. IEEE Geosci Remote Sens Lett 16(4):623–627

Yuan SY, Liu Y, Zhang Z, Luo CM, Wang SX (2019b) Prestack stochastic frequency-dependent velocity inversion with rock-physics constraints and statistical associated hydrocarbon attributes. IEEE Geosci Remote Sens Lett 16(1):140–144

Zhong JG, Huang Y (2010) Time–frequency representation based on an adaptive short-time Fourier transform. IEEE Trans Signal Process 58(10):5118–5128